

# Visual-Inertial Sensor Fusion with a Bio-Inspired Polarization Compass for Navigation of MAVs

Florian Steidle\*, Wolfgang Stürzl, Rudolph Triebel  
Institute of Robotics and Mechatronics, German Aerospace Center (DLR), Germany

## ABSTRACT

We present the integration of a polarization compass in a visual-inertial sensor fusion framework onboard a Micro Aerial Vehicle (MAV). The polarization compass estimates the position of the sun indirectly from the pattern of skylight polarization even in cases where the sun is not visible. It is based on a polarization sensor which consists of a standard RGB camera and a small polarizing unit that creates three polarization images on the camera sensor. Due to its low weight and compact size it is ideally suited for small aerial systems. The readings from the polarization compass are fused with angular rate and acceleration measurements from an Inertial Measurement Unit (IMU) and the 6 Degrees of Freedom (DOF) pose changes from the Visual Odometry (VO) in an indirect extended Kalman filter (EKF). Two different approaches to integrate the readings from the polarization compass in the filter are presented and compared. We show in experiments that adding a compass to visual-inertial sensor fusion does not only eliminate the drift of yaw angle estimates but also improves overall state estimation of the system.

## 1 INTRODUCTION

Due to the complementary information they provide, the fusion of visual and inertial data is widely used for state-estimation of MAVs, in particular in environments where global navigation satellite systems (GNSS) are unavailable or unreliable. While it is possible to estimate absolute roll and pitch angles based on acceleration measurements, the yaw angle is subject to drift as it can only be estimated by continuously integrating orientation differences. Therefore, magnetometers are often added. By measuring the magnetic field of the Earth, the absolute yaw angle can be estimated. In this case all degrees of rotation are observable, as well as the angular velocity and acceleration biases, which results in higher overall accuracy of the system. However, magnetic compasses can be disturbed by magnetic objects or electrical devices. Beside the magnetic field of the earth the position of the sun can be used as a compass cue and even if the sun is not directly visible its position can be estimated indirectly via the

\*Email address: florian.steidle@dlr.de



Figure 1: Multicopter “ARDEA” with a frame in triangle shape, three pairs of counter-rotating rotors and a sensor suite mainly consisting of an IMU, two pairs of wide-angle stereo cameras and an insect-inspired polarization compass (highlighted by red ellipse).

polarization pattern of the sky light. An other advantage compared to a magnetic compass is its insensitivity to interference fields caused, for instance, by electric devices. This motivated us to equip our multicopter “ARDEA” [7] with a bio-inspired polarization sensor and integrate its compass measurements in our Visual Inertial Navigation System (VINS).

In [1] a polarization compass was fused with IMU readings, but VOs were not used, the measurement equation for the polarization is different and instead of an indirect EKF a complementary filter was used. In [2] accelerations and angular rates are fused with readings from a polarization compass in a Kalman filter. But they also used readings from a GNSS and only estimated the orientation of their device.

The main contributions of our approach are a system for pose estimation onboard a MAV which does neither depend on external infrastructure nor readings of the magnetic field and nonetheless can provide a drift-free 3 DOF orientation estimate. Its accuracy is improved in comparison to a pure VINS and it avoids the usage of 3 DOF measurements of the direction vector to the sun with almost singular covariance matrix by projecting the measurement errors to different two dimensional subspaces.

In the following we describe the polarization compass in Section 2, the approach to combine data from different sensors in Section 3, the experiments in Section 4 and finally conclude the paper with Section 5.

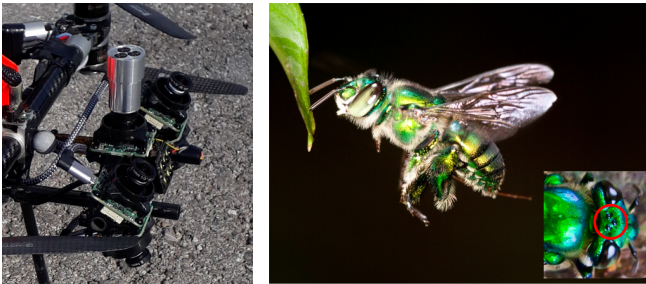


Figure 2: The polarization sensor, a standard camera with cylindrical polarizer unit mounted in front of the camera lens is positioned between the two stereo camera pairs (left). The sensor was inspired by the ocelli of orchid bees. As highlighted by the red circle in the inset of the right figure (shown is a close up view of the head of the bee *Euglossa imperialis*), bees have three simple eyes with polarization sensitive photoreceptors (photos courtesy of Emily Baird, Stockholm University). In orchid bees, the preferred polarization orientation is very similar within each eye but differs between eyes by somewhat less than  $60^\circ$  [3].

## 2 POLARIZATION COMPASS

We briefly describe the polarization sensor and summarize the computation of the sun vector. For more details see [4]. The polarization sensor utilized on our multicopter is identical to the one described in [4] except for the camera sensor. It is replaced by an USB3 camera with Sony IMX265 CMOS color sensor (IDS UI 3271LE-C).

### 2.1 Sky polarization pattern as compass cue

Scattering of sun light in the atmosphere creates a characteristic polarization pattern in the sky that is essentially symmetric with respect to the position of the sun. The degree of polarization is low close to the sun, increases with angular distance from the sun up to  $90^\circ$  and decreases for larger angles. Measuring the polarization, in particular its orientation, which is known to be more reliable than the degree of polarization [5], even just for small regions of the sky allows to estimate the sun position or at least its azimuth in cases where the sun is occluded by clouds, trees or buildings. Therefore, similar to the sun, the polarization pattern can be used as a compass. Interestingly, insects are known to use both, direct sun position and polarization pattern for orientation [6]. Bees and many other insect species, like desert ants, have a specialized region in the upper part of their compound eyes that are sensitive to polarization. In addition, there is recent evidence that the three simple eyes of bees located at the top of the head in between the two compound eyes, the “ocelli” (see right sub figure of Figure 2), might also play a role in polarization sensing. While each ocellum contains photoreceptors of similar preferred orientation, the preferred orientations of all three ocelli differ strongly. This arrangement of polarization sensitive photoreceptors in bees inspired the polarization

sensor design and its use as compass cue on our multicopter ARDEA. As sky light is predominantly linearly polarized, i.e. contains almost no circular or elliptical polarization, three is the minimum number of linear polarizers sufficient for estimating all relevant polarization parameters.

### 2.2 Polarization sensor and multi-camera setup on MAV

As shown in Figure 1 and 2 the polarization sensor is placed between Ardea’s “compound eyes” that consist of two wide-angle cameras on either side. The arrangement of these cameras provides a very large stereo FOV of approx.  $240^\circ$  vertically. As described in [7], each wide-angle camera is remapped to two virtual pinhole cameras to allow for efficient image processing.

The polarization sensor consists of a standard camera with a small-aperture lens to which the cylindrical polarizer unit is attached, see Figure 2. By means of this unit the camera image contains three basically identical images of the sky seen through three differently oriented linear polarizers (Figure 3 left). The preferred polarization orientations differ by  $60^\circ$ .

In contrast to several devices based on photodiodes, e.g. [8, 9], the polarization sensor allows to estimate a large number of polarization vectors, which – in combination with a comparatively large field of view of approx.  $56^\circ$  – enables the estimation of the “sun vector”, i.e. not only the azimuth of the sun but also its elevation angle can be inferred.

### 2.3 Remapping and polarization estimation

Raw images of the polarization camera of size  $800 \times 800$  pixels are de-bayered, scaled down by factor 0.5 and then remapped to three polarization images ( $120 \times 120$  pixels) with constant radial resolution of  $0.5^\circ$  per pixel. From the intensity differences of corresponding pixels, i.e. pixels with same viewing directions as estimated by a three-camera-calibration using the DLR-CalDe/CalLab tool [10], the angle  $\phi$  and degree of polarization  $\delta$  can be determined for each pixel of the reference image (the remapped sub-image ‘1’), see [4] for details. By retracing the pixel rays, the polarization orientation on the sky sphere can be computed, which we describe by the 3D unit vector  $\pm \mathbf{f}_i$  in the following, where  $i$  is the index of the pixel with image coordinates  $(u_i, v_i)$ . If the multicopter is aligned with the north direction then the  $u$ -axis of the camera image points towards the west and the  $v$ -axis towards the south (see p-frame in Figure 4). The exact transformation between the polarization camera frame and the IMU or body frame of the multicopter was estimated based on an extrinsic calibration of the polarization camera and the topmost left virtual pinhole camera and an IMU-to-camera calibration between the reference pinhole camera and the IMU.

## 2.4 Sun vector estimation

As described in [4], the sun vector  ${}^p\mathbf{p}_s$  can be estimated by minimizing

$$E({}^p\mathbf{p}_s) = \sum_i \tilde{w}_i (\pm \mathbf{f}_i^\top \mathbf{p}_s)^2 = {}^p\mathbf{p}_s^\top \left( \sum_i \tilde{w}_i \mathbf{f}_i \mathbf{f}_i^\top \right) {}^p\mathbf{p}_s \quad (1)$$

under the constraint  $\|{}^p\mathbf{p}_s\| = 1$ .  $\tilde{w}_i = (\sum_k w_k)^{-1} w_i$  are normalized weights. The weights  $w_i$  basically depend on the degree of polarization and the “blueness” of the corresponding pixel favoring “sky-pixels”. Equation 1 is motivated by the fact that ideally all polarization vectors  $\{\mathbf{f}_i\}$  are orthogonal to the observer-sun axis, i.e. the sun vector  ${}^c\mathbf{p}_s$ . Pre-whitening [11] of matrix  $\mathbf{P} = \sum_i \tilde{w}_i \mathbf{f}_i \mathbf{f}_i^\top$  is used to reduce the bias that would result from solving the eigenvalue problem defined in Equation 1 directly. Assuming independent and identically distributed errors with standard deviation  $\sigma$ , the covariance matrix of the sun vector can be estimated,

$$\Sigma_{{}^p\mathbf{p}_s} \approx \sigma^2 \mathbf{Q} \sum_i \tilde{w}_i^2 (1 - ({}^p\mathbf{p}_s^\top \mathbf{e}_i)^2) \mathbf{f}_i \mathbf{f}_i^\top \mathbf{Q}^\top \quad (2)$$

$\mathbf{Q}$  is a matrix describing rotation, scaling and projection onto the plane orthogonal to the estimated sun vector, and  $\mathbf{e}_i$  is the viewing direction of pixel  $i$ .

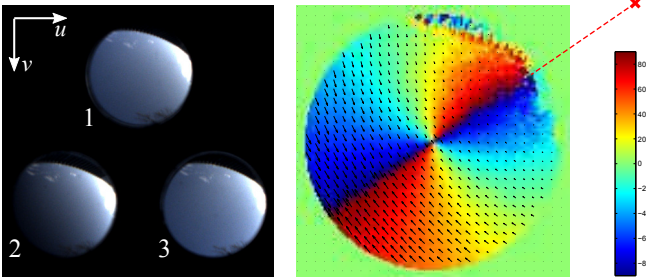


Figure 3: Estimation of sun position from the three images of the polarization sensor. Left: The camera image containing the three sub-images after de-bayering. In this example the sun is located outside the field of view of the camera. A bright cloud visible in the upper right corner of the sub-images indicates the approximate sun direction. Intensity differences between the three sub-images allow to estimate polarization degree and angle for each pixel. For example, quite strong intensity differences can be observed in the lower left corner of the three sub-images indicating high degree of polarization. Right: Shown are the sky polarization angles, i.e. the angles of the polarization vectors with respect to the local meridians (great circles of constant azimuth) in color code, ranging from  $-90^\circ$  (blue) to  $+90^\circ$  (red), and polarization vectors  $\mathbf{f}_i$  with length scaled according to weight  $w_i$  (black arrows), projected onto the image plane. The red cross in the upper right corners depicts the estimated position of the sun (approx.  $-34.5^\circ$  azimuth and  $+36^\circ$  elevation angle with respect to the camera frame).

## 3 FUSION

### 3.1 Extended Kalman filter based visual-inertial odometry

In [12] and [13] an indirect, extended Kalman filter was introduced that combines the readings from an IMU and a single VO. In [7] the filter was extended to cope with multiple VOs.

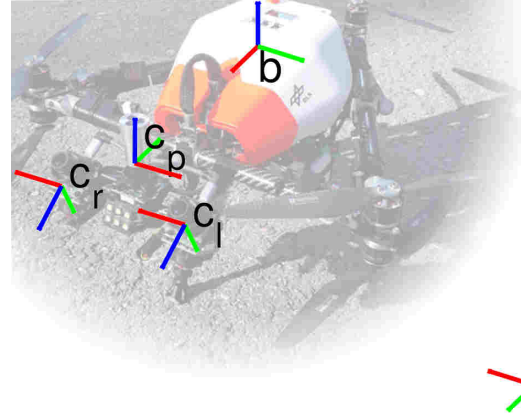


Figure 4: An image of ARDEA with the navigation frame (n-frame), the body frame (b-frame), the frames of one stereo pair ( $c_1$ - and  $c_r$ -frame) and the frame of the camera with the polarization compass (p-frame).

The main state  $\mathbf{x}$  of the filter is defined by

$$\mathbf{x} = [{}^n\mathbf{p}^\top \quad {}^n\mathbf{v}^\top \quad {}^n\mathbf{q}^\top \quad {}^b\mathbf{b}_a^\top \quad {}^b\mathbf{b}_\omega^\top]^\top, \quad (3)$$

with the position  ${}^n\mathbf{p} \in \mathbb{R}^3$  of the body frame (b-frame) relative to an earth-fixed, inertial frame (n-frame), the velocity  ${}^n\mathbf{v} \in \mathbb{R}^3$ , the orientation  ${}^n\mathbf{q} \in \mathbb{R}^4$  represented by a unit quaternion and the acceleration  ${}^b\mathbf{b}_a \in \mathbb{R}^3$  and angular rate  ${}^b\mathbf{b}_\omega \in \mathbb{R}^3$  biases of the IMU. The relationship between the main coordinate systems involved is shown in Figure 4.

If a raw measurement from a sensor is taken, its transmission and processing needs time and is therefore delayed when the results are available to the filter. For some sensors, e.g. IMUs the delay can often be neglected, for other sensors, e.g. cameras the delay usually has to be taken into account. Therefore, parts of the main state that are necessary to process the delayed measurements, when they arrive have to be augmented to the state. The final state consists of the main state  $\mathbf{x}$  and an arbitrary number of augmented states  $\mathbf{x}_{\text{aug}}$ .

A measurement from the VO that becomes available at time  $t_k$  can be described by

$$\mathbf{h}_k = \mathbf{h}(\mathbf{x}_{k-n}, \mathbf{x}_{k-m}), \quad (4)$$

where the states at time  $t_{k-n}$  and  $t_{k-m}$  must be part of the augmented state.

Instead of estimating the state directly, it is possible to estimate the errors of the state. This has several advantages, e.g. system dynamics can be decoupled from error dynamics, a

sophisticated model of the system is not needed and rotation errors can be locally described with a minimal representation. The indirect formulation is given by

$$\delta \mathbf{x} = \begin{bmatrix} {}^n_b \delta \mathbf{p}^\top & {}^n_b \delta \mathbf{v}^\top & {}^n_b \delta \phi^\top & {}^b_b \delta \mathbf{b}_a^\top & {}^b_b \delta \mathbf{b}_\omega^\top \end{bmatrix}^\top, \quad (5)$$

where all errors are in the form of  ${}^n_b \hat{\mathbf{p}} = {}^n_b \mathbf{p} + {}^n_b \delta \mathbf{p}$ , except the orientation error, which has an multiplicative error definition  ${}^n_b \hat{\mathbf{q}}_b = {}^n_b \mathbf{q}_b \otimes {}^n_b \delta \mathbf{q}_n$ . The quaternion multiplication is denoted by  $\otimes$  and  ${}^n_b \delta \mathbf{q}_n$  is the error quaternion corresponding to the angular error  $\delta \phi$ .

### 3.2 Extending the EKF with readings from a polarization compass

The polarization compass determines the direction vector  ${}^p \bar{\mathbf{p}}_s \in \mathbb{R}^3$  pointing to the sun expressed in the frame of the polarization camera (p-frame) and its corresponding covariance matrix  $\Sigma_s \in \mathbb{R}^{3 \times 3}$ .

Using the convention to indicate the spherically normalized version of a vector  $\mathbf{p}$  by  $\bar{\mathbf{p}} = \frac{\mathbf{p}}{\|\mathbf{p}\|}$ , the equation to transform the position of the sun in the navigation frame  ${}^n \mathbf{p}_s$  to the camera frame  ${}^p \mathbf{p}_s$  is given by (see [14])

$${}^p \bar{\mathbf{p}}_s = {}^c \mathbf{R}_b {}^b \mathbf{R}_n {}^n \bar{\mathbf{p}}_s. \quad (6)$$

The relation between the error of the expected measurement  $\hat{\mathbf{h}}$  and the actual measurement  $\mathbf{h}_m$  as well as the error of the system state  $\delta \mathbf{x}$  have to be defined in order to use them in the filter,

$$\begin{aligned} \delta \mathbf{h} &= \mathbf{\Pi}(\hat{\mathbf{h}} - \mathbf{h}_m) \\ &= \mathbf{\Pi}({}^p \mathbf{R}_b {}^b \mathbf{R}_n {}^n \bar{\mathbf{p}}_s - {}^p \mathbf{R}_b {}^b \mathbf{R}_n {}^n \bar{\mathbf{p}}_s) \\ &= \mathbf{\Pi}({}^p \mathbf{R}_b {}^b \mathbf{R}_n {}^n \bar{\mathbf{p}}_s - {}^p \mathbf{R}_b {}^b \mathbf{R}_n (\mathbf{I}_{3 \times 3} + [\delta \phi]_\times) {}^n \bar{\mathbf{p}}_s) \\ &= \mathbf{\Pi} {}^p \mathbf{R}_b {}^b \mathbf{R}_n [{}^n \bar{\mathbf{p}}_s]_\times \delta \phi. \end{aligned} \quad (7)$$

To solve Equation 7 the true rotation from the navigation frame to the body frame  ${}^b \mathbf{R}_n$  is unknown and can be approximated by  ${}^b \mathbf{R}_n = {}^b \mathbf{R}_n (\mathbf{I}_{3 \times 3} + [\delta \phi]_\times)$ . The matrix  $\mathbf{\Pi}$  is a projection matrix. It can be set to a constant value, e.g.  $\mathbf{\Pi}_s = \begin{bmatrix} 1 & 0 & 0 \\ 0 & 1 & 0 \end{bmatrix}$ , which maps the angular error  $\delta \phi$  to the  $x$ - $y$ -plane of the polarization camera. If the deviation between the sun vector and the  $z$ -axis of the camera is sufficiently small, the performance will be satisfactory. Given the dynamics of the system and the fact, that the sun vector changes during the day, improvements can be expected by adapting  $\mathbf{\Pi}_d$  dynamically. By projecting the error between the predicted and measured sun vector onto the tangent space on the sphere at the predicted sun vector, the measurement error is invariant with respect to the estimated orientation [15]. The tangent space to the unit sphere is spanned by the column vectors of the matrix

$$\mathbf{\Pi}_d = \mathcal{N}({}^p \bar{\mathbf{p}}_s^\top) = [\mathbf{s}_{1\perp} \quad \mathbf{s}_{2\perp}]^\top, \quad (8)$$

where  $\mathcal{N}({}^p \bar{\mathbf{p}}_s^\top)$  denotes the left null space of the vector  ${}^p \bar{\mathbf{p}}_s$ . The matrix  $\mathbf{\Pi}_d$  has to fulfill the property  $\mathbf{\Pi}_d \mathbf{\Pi}_d^\top = \mathbf{I}_2$ . One possible solution is given by

$$\begin{aligned} \mathbf{s}_{1\perp} &= \frac{1}{\sqrt{\bar{p}_{s,x}^2 + \bar{p}_{s,y}^2}} [-\bar{p}_{s,y} \quad \bar{p}_{s,x} \quad 0]^\top, \\ \mathbf{s}_{2\perp} &= \frac{1}{\sqrt{\bar{p}_{s,x}^2 + \bar{p}_{s,y}^2}} [-\bar{p}_{s,x} \bar{p}_{s,z} \quad -\bar{p}_{s,y} \bar{p}_{s,z} \quad \bar{p}_{s,x}^2 + \bar{p}_{s,y}^2]^\top. \end{aligned} \quad (9)$$

In the case of a static projection matrix, the covariance estimate  $\Sigma_s$  can be projected to the subspace by the equation

$$\Sigma_{s,r} = \mathbf{\Pi}_s \Sigma_s \mathbf{\Pi}_s^\top. \quad (10)$$

In the case of a dynamic projection matrix, the static projection matrix  $\mathbf{\Pi}_s$  has to be replaced with the matrix  $\mathbf{\Pi}_d$  defined in Equation 8 and Equation 9. The reduced covariance matrix  $\Sigma_{s,r} \in \mathbb{R}^{2 \times 2}$  is non-singular and can be used in the filter update equations.

## 4 EXPERIMENTS

Several experiments were carried out to test the different components of the system under varying conditions. The set of indoor experiments was done in a lab where high frequency ground truth data was available, but readings of the polarization sensor had to be simulated. For the set of outdoor experiments ground truth data was only available occasionally but real readings from the polarization sensor could be used.

The set of indoor experiments consists of a trajectory of ARDEA, which was augmented with simulated readings of the polarization compass to evaluate the influence of the polarization compass. The set of outdoor experiments consists of one experiment to evaluate the performance of the polarization compass itself and a second experiment to evaluate the performance of the overall system.

### 4.1 Test of the polarization compass

As an initial test, we placed the multicopter on a leveled turntable and recorded the estimated sun azimuth and elevation angles while turning the multicopter in steps of  $30^\circ$ . As illustrated in Figure 5, the sun position can be determined quite accurately with a standard deviation below  $1^\circ$  for azimuth and below  $3^\circ$  for elevation angle.

### 4.2 Indoor test of pose estimation with simulated measurements from the polarization compass

In the second experiment a trajectory of an indoor experiment in the lab was augmented with simulated measurements of the polarization compass. The measurements of the polarization compass were artificially corrupted by zero mean, white Gaussian noise. The noise levels were empirically determined. For the indoor datasets at each time stamp the ground truth pose of ARDEA is available with high precision.

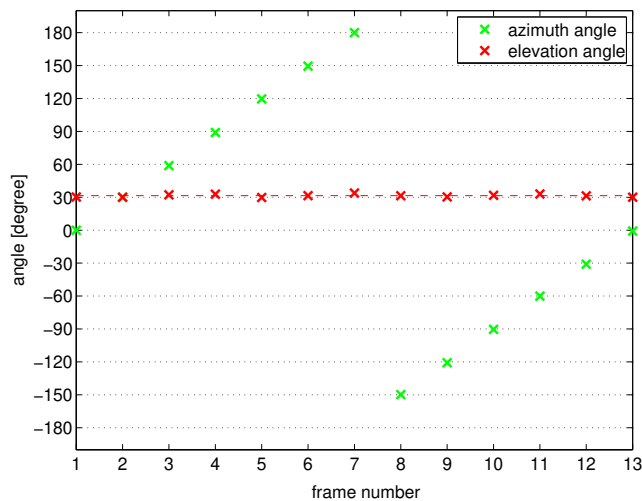


Figure 5: Test of the sun position estimation by turning the multicopter in  $30^\circ$  steps. Shown are the azimuth angle with respect to the initial orientation (green 'x') and the sun elevation angles (red 'x') as estimated by the polarization compass. The dashed line shows the true sun elevation angle ( $\approx 32^\circ$ ).

Therefore, Euler angle errors can be calculated. They are depicted in Figure 6. Roll and pitch errors stay limited for all three cases, while the yaw angle error grows unbounded with time if the polarisation compass is not used. Due to the use of the polarization compass its steady increase can be compensated.

#### 4.3 Outdoor test of pose estimation with real measurements from the polarization compass

In Figure 7 the estimated position of ARDEA during an outdoor experiment is given. The start and final positions are at the origin. The polarization compass improves the estimates in the case of the dynamic projection matrix  $\Pi_d$  and also in the case of the static projection matrix  $\Pi_s$ . Slight differences between the static and dynamic projection approach can be seen for the  $z$ -direction, where the dynamic projection results in a lower error.

An often used error metrics for translational errors is the norm of the distance of the estimated final position to the true final position with respect to trajectory length. Given the length of the trajectory of approx. 132 m, the relative errors are 2.7%, 0.6% and 0.5% for the approach without the polarization compass, with the polarization compass and a static projection matrix and with the polarization compass and dynamic projection matrices.

Roll and pitch angles are globally observable when fusing accelerometer and gyroscope readings with the delta poses of a VO. Therefore, the polarization compass only slightly improves their estimation. But the slight improvement of roll and pitch estimation results in a lower vertical position error. Without the polarization compass, the yaw angle error grows

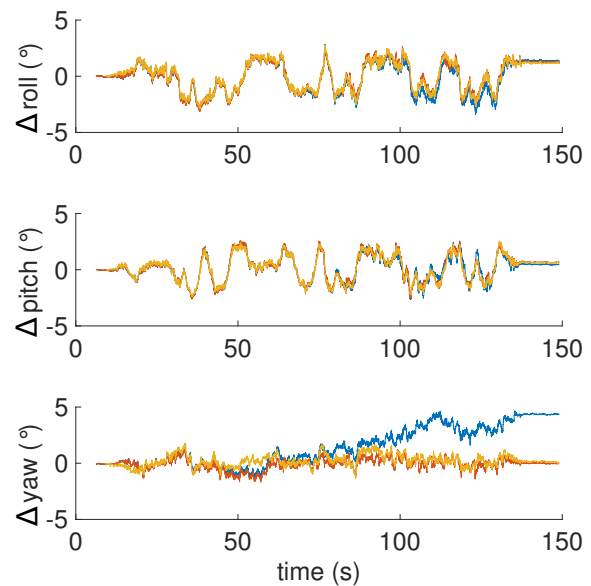


Figure 6: Roll, pitch and yaw error for a single run with simulated sun vector measurements. Blue: without polarization compass, red: with polarization compass using static projection, yellow: with polarization compass using dynamic projection.

unbounded with time. Due to the polarization compass this drift can be compensated, which results in improvements of  $x$  and  $y$  position estimates.

Multiple runs with different trajectories resulted in similar system behavior and similar values of the error metrics.

## 5 CONCLUSIONS

It was shown in the experiments that fusing the polarization compass with the data from an inertial measurement unit and a VO in an indirect EKF improves the accuracy of pose estimation. The differences are small between the approach with a static projection matrix and a dynamic projection matrix. While a polarization compass can obviously provide orientation estimations only outdoors, it is likely to improve state estimation also in mixed indoor/outdoor flights. Furthermore, using a polarization compass in conjunction with a VINS could also be beneficial in other applications, e.g. when matching maps from multiple robots.

## REFERENCES

- [1] R. Jin, H. Sun, J. Sun, W. Chen, and J. Chu. Integrated navigation system for UAVs based on the sensor of polarization. In *ICMA*, pages 2466–2471, 2016.
- [2] W. Zhi, J. Chu, J. Li, and Y. Wang. A novel attitude determination system aided by polarization sensor. *Sensors*, 18(1):158, 2018.
- [3] G. J. Taylor, W. Ribi, M. Bech, A. J. Bodey, C. Rau, A. Steuwer, E. J. Warrant, and E. Baird. The dual func-

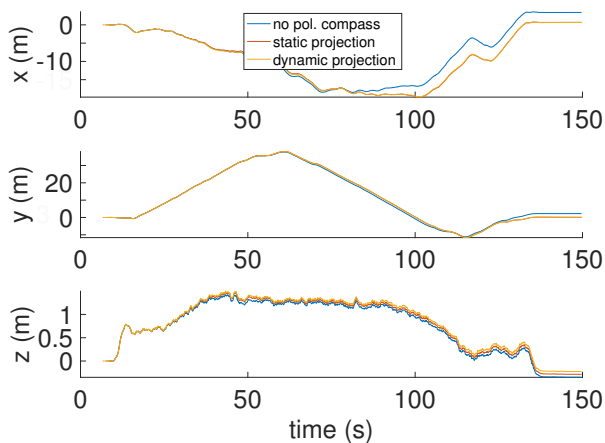


Figure 7: Estimated position of ARDEA during an outdoor experiment with and without the polarization compass.

tion of orchid bee ocelli as revealed by x-ray microtomography. *Current Biology*, 26(10):1319–1324, 2016.

- [4] W. Stürzl. A lightweight single-camera polarization compass with covariance estimation. In *ICCV*, pages 5363–5371, 2017.
- [5] G. Horváth and D. Varjú. *Polarized Light in Animal Vision: Polarization Patterns in Nature*. Springer, 2004.
- [6] R. Wehner and M. Mueller. The significance of direct sunlight and polarized skylight in the ant’s celestial system of navigation. *Proceedings of the National Academy of Sciences of the United States of America*, 103:12575–12579, 2006.
- [7] M. G. Müller, F. Steidle, M. Schuster, P. Lutz, M. Maier, S. Stoneman, T. Tomic, and W. Stürzl. Robust visual-inertial state estimation with multiple odometries and efficient mapping on an MAV with ultra-wide FOV stereo vision. In *IROS*, 2018.
- [8] D. Lambrinos, R. Möller, T. Labhart, R. Pfeifer, and R. Wehner. A mobile robot employing insect strategies for navigation. *Robotics and Autonomous Systems*, 30:39–64, 2000.
- [9] J. Chahl and A. Mizutani. Biomimetic attitude and orientation sensors. *IEEE Sensors Journal*, 12:289–297, 2012.
- [10] K. H. Strobl, W. Sepp, S. Fuchs, C. Paredes, M. Smisek, and K. Arbter. DLR CalDe and CalLab, [www.robotic.dlr.de/callab/](http://www.robotic.dlr.de/callab/). Institute of Robotics and Mechatronics, German Aerospace Center (DLR).
- [11] W. J. MacLean. Removal of translation bias when using subspace methods. In *ICCV*, pages 753–758, 1999.
- [12] K. Schmid, F. Ruess, M. Suppa, and D. Burschka. State estimation for highly dynamic flying systems using key frame odometry with varying time delays. In *IROS*, pages 2997–3004, 2012.
- [13] K. Schmid, F. Ruess, and D. Burschka. Local reference filter for life-long vision aided inertial navigation. In *Fusion*, 2014.
- [14] N. Trawny and S. Roumeliotis. Sun sensor model. *University of Minnesota, Dept. of Comp. Sci. & Eng., Tech. Rep*, 1, 2005.
- [15] W. Förstner. Minimal representations for uncertainty and estimation in projective spaces. In *ACCV*, pages 619–632, 2010.